ACS Photonics

pubs.acs.org/journal/apchd5

Article

Light Modulation in Silicon Photonics by PZT Actuated Acoustic Waves

Irfan Ansari, John P. George, Gilles F. Feutmba, Tessa Van de Veire, Awanish Pandey, Jeroen Beeckman, and Dries Van Thourhout*

Cite This: *ACS Photonics* 2022, 9, 1944−1953

Read Online

ACCESS | Metrics & More | Article Recommendations | Supporting Information

ABSTRACT: Tailoring the interaction between light and sound has opened new possibilities in photonic integrated circuits (PICs) that range from achieving quantum control of light to high-speed information processing. However, the actuation of sound waves in Si PICs usually requires integration of a piezoelectric thin film. Lead zirconate titanate (PZT) is a promising material due to its strong piezoelectric and electromechanical coupling coefficient. Unfortunately, the traditional methods to grow PZT on silicon are detrimental for photonic applications due to the presence of an optical lossy intermediate layer. In this work, we report integration of a high quality PZT thin film on a silicon-on-insulator (SOI) photonic chip using an optically transparent buffer layer. We demonstrate acousto-optic modulation in silicon waveguides with the PZT actuated acoustic waves. We fabricate interdigital transducers (IDTs) on the PZT film with a contact photolithography and electron-beam lithography to generate the acoustic waves in MHz and GHz ranges, respectively. We obtain a $V_\pi L \sim 3.35$ V·cm at 576 MHz from a 350 nm thick gold (Au) IDT with 20 finger-pairs. After taking the effect of mass-loading and grating reflection into account, we measured a $V_\pi L \sim 3.60$ V·cm at 2 GHz from a 100 nm thick aluminum (Al) IDT consisting of only four finger-pairs. Thus, without patterning the PZT film nor suspending the device, we obtained figures-of-merit comparable to state-of-the-art modulators based on SOI, making it a promising candidate for a broadband and efficient acousto-optic modulator for future integration.

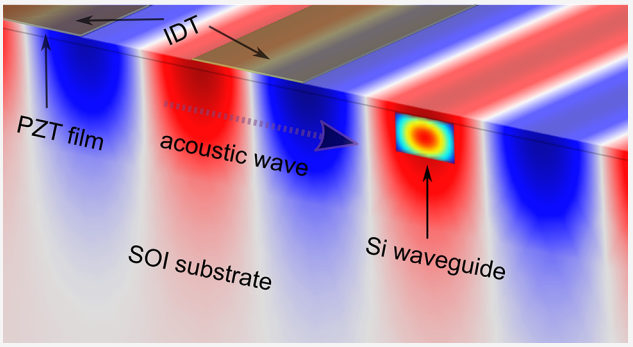

KEYWORDS: *surface acoustic wave, PZT, silicon photonics, acousto-optic modulator, optomechanics*

INTRODUCTION

Light−sound interaction in integrated waveguide systems has enabled a wide-range of photonic applications ranging from microwave photonics filters,[1,2] isolators,[3−5] modulators,[6−13] mode-shifters,[14−16] nonreciprocal light transmission,[17−20] and frequency comb generation[21−23] to quantum state control and quantum information processing.[24−28] These devices harness the large overlap between the tightly confined light in a nanophotonic waveguide and acoustic phonons associated with a mechanical vibration. Demonstrations of such acousto-optic interactions in $LiNbO_3$,[12,13,29−31] GaAs,[28,32−34] and InP[35,36] based integrated photonics platforms have been reported over the last years. However, on the silicon photonics platform, progress in this field has been lagging as silicon does not exhibit a piezo-electric effect. Overcoming this deficiency would be a stepping stone toward realizing novel photonic applications, as the silicon photonics platform is rapidly gaining maturity and already offers a remarkable range of high-performance building blocks, including modulators, filters, isolators, detectors, and lasers. Moreover, its compatibility with CMOS technology offers a route toward mass manufacturing and commercialization.[37,38]

Recently, thermoelastic actuation of acoustic waves on SOI was reported.[39,40] However, such a scheme is power-hungry due to the need of a high power modulated pump source and is costly, as they need separate electro-optic modulators. Therefore, a more promising route involves the direct integration of piezoelectric materials on the SOI platform. For instance, AlN has been integrated with silicon waveguides[41] and used to demonstrate an electrically driven acousto-optic modulator on SOI.[20] This inspired the investigation of other materials exhibiting a strong piezoelectric effect that can be integrated with Si PICs.

Received: December 4, 2021
Published: May 20, 2022

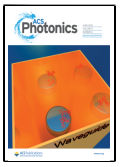

Lead zirconate titanate (PZT) is one of the most widely used piezoelectric ceramic materials due to its strong piezoelectricity, high electromechanical coupling coefficient, common availability, and high temperature compatibility (Curie point ~ 370 °C).[42−44] Hence, integration of a highly textured PZT thin film on SOI could be a promising alternative for realizing efficient optomechanical interactions in Si PICs. However, PZT thin films have traditionally been grown using a Pt seed layer, making them incompatible with photonic technology due to the high optical loss.[45] Although PZT films sandwiched between two Pt electrodes have been successfully used to obtain stress-optic phase modulation,[46] the modulation speed was limited to about 5 kHz.

Recently, a novel approach for integrating highly textured PZT-films has been developed, using a thin and transparent lanthanide based buffer layer.[47] The high quality of this PZT film has been proven through the demonstration of electro-optic modulators with very low optical loss (<1 dB/cm) on both SiN[48] and Si photonic platforms.[49] Additionally, we also demonstrated that this film exhibits a high second-order nonlinearity (χ^2_{zzz} 128 pm/V).[50] Therefore, a detailed investigation of the piezoelectric effect and acousto-optic modulation with this PZT film is warranted.[51−53]

In this work, we give a brief theoretical description of the acousto-optic interaction in a waveguide, followed by simulation of the acoustic wave actuation with an interdigital transducer (IDT). Then we experimentally show the piezoelectric actuation of a surface acoustic wave (SAW) by an IDT fabricated on a PZT-on-glass substrate. Finally, we integrate the PZT thin film on an SOI photonic chip (as shown in Figure 1) and demonstrate acousto-optic modulation in a Si

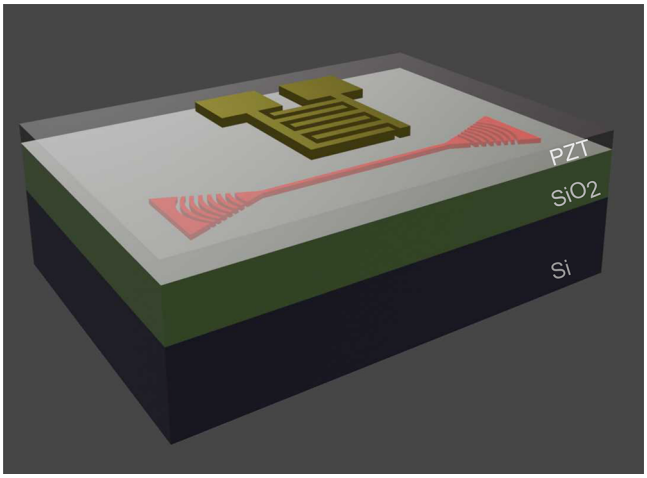

Figure 1. 3D drawing of a typical IDT fabricated on a SOI photonic chip. The Si waveguide is embedded between the PZT layer and the SiO_2 cladding.

waveguide using an Au IDT. We thereafter present a computational analysis on the effect of the IDT thickness made of a dense metal Au on the transduction efficiency. In the next progression, we use a thinner and lighter metal Al IDT with a smaller period and demonstrate GHz light modulation with a figure-of-merit comparable to state-of-the-art electro-optic[48] and acousto-optic modulators.[20,33,54] Thus, we report the first acousto-optic modulator realized through the direct integration of a photonic compatible PZT thin film on the SOI platform.

ACOUSTIC WAVE GENERATION

A surface acoustic wave (SAW) is launched by creating a time-varying periodic deformation pattern along the surface of an elastic material.[55] The propagating SAW is confined near the surface in a region with an extent in the order of its wavelength. The wavelength of the primary SAW mode is equal to the grating period, and its resonance frequency is determined by the acoustic phase velocity of the medium and the boundary condition (free surface).[56,57]

Thermoelastic actuation of a SAW has been shown,[39,40,58−60] but in general, electromechanical actuation[61] is preferred due to its convenience and efficieny. In this method, an IDT consisting of a periodic electrode pattern is deposited on a piezoelectric material. The electrode pairs in the IDT allow the generation of alternate electric fields in the piezoelectric material, which then results in a periodic strain profile. Upon actuation of a piezoelectric material with an IDT, also leaky-SAW modes can be actuated. However, this type of waves suffer more from viscous damping in the bulk medium. The leaky-SAW resonance frequency is determined by the IDT-grating period and the longitudinal bulk acoustic velocity of the elastic medium. For a given IDT period, this resonance frequency is usually higher than the SAW resonance frequency (as the longitudinal bulk velocity > SAW velocity).[56,62−64]

SIMULATION OF THE ACOUSTIC WAVE ACTUATION IN PZT

The macroscopic behavior of a polycrystalline PZT film is determined by the net crystallographic orientation of its domains.[65] The polarization of these domains can be aligned by applying a sufficiently high electric field (the poling process).

In Figure 2, we show how the electromechanical actuation depends on the PZT domain polarity. We consider three

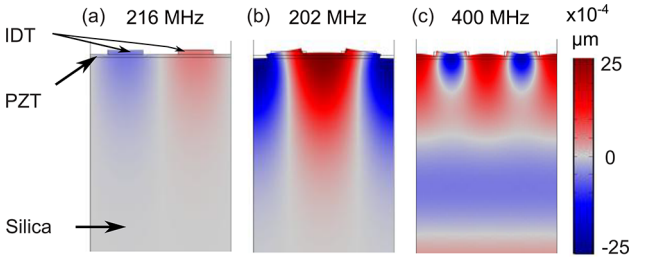

Figure 2. 2D finite element method (FEM) simulation shows the vertical displacement from the SAW actuation for three PZT domain polarities: (a) out of the substrate plane, (b) uniformly in-plane, perpendicular to the IDT fingers, and (c) periodically oriented along the IDT electric field lines.

different configurations: (a) out-of-plane polariztion, (b) uniform in-plane polarization, perpendicular to the IDT-electrodes, and (c) polarization periodically oriented along the electric field lines applied by the IDT. We notice that the resulting displacement is much weaker with the out-of-plane oriented PZT domains (a) compared to the in-plane oriented PZT domains (b, c). This can be explained from the inverse piezoelectric tensor for PZT. From the piezoelectric constitutive equation, the induced strain is determined as[66]

https://doi.org/10.1021/acsphotonics.1c01857
ACS Photonics 2022, 9, 1944−1953

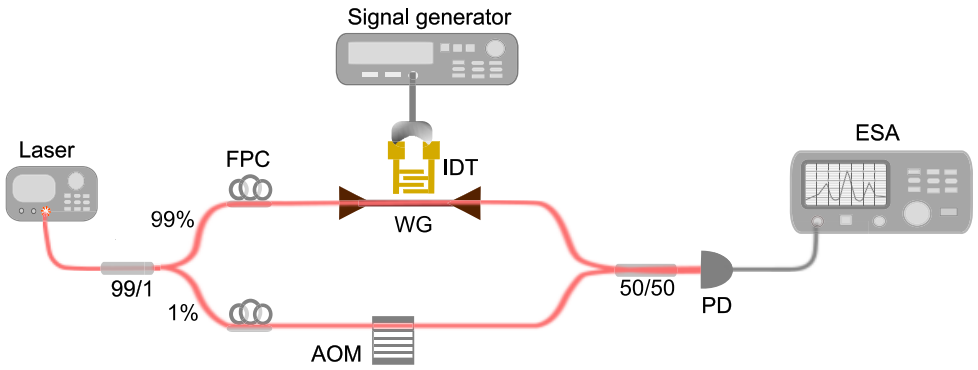

Figure 3. Schematic of the heterodyne setup used to measure the acousto-optic phase modulation. A commercial acousto-optic modulator (AOM) was used as a local oscillator to frequency shift the reference signal by 200 MHz. This frequency shifted signal was then mixed with the phase modulated signal emerging of the DUT via a 3 dB fiber combiner to down-convert the carrier signal on a detector.

$$\begin{bmatrix} S_1 \\ S_2 \\ S_3 \\ S_4 \\ S_5 \\ S_6 \end{bmatrix} = \begin{bmatrix} 0 & 0 & d_{31} \\ 0 & 0 & d_{31} \\ 0 & 0 & d_{33} \\ 0 & d_{24} & 0 \\ d_{15} & 0 & 0 \\ 0 & 0 & 0 \end{bmatrix} \begin{bmatrix} E_x \\ E_y \\ E_z \end{bmatrix}$$

where d_{ij} is the tensor describing the inverse piezoelectric effect for PZT and E_i is the applied electric field. In the simulation, we used the following inverse-piezoelectric coefficients for PZT: $d_{31} = -171$ pm/V, $d_{33} = 374$ pm/V, and $d_{15} = d_{24} = 584$ pm/V.[67]

From this relation we see that, for a longitudinal actuation of PZT (necessary to launch a SAW), the applied electric field should be along the z-axis (E_z) in the crystal coordinate system, that is, along the PZT domain polarization. Therefore, in order to have an effective SAW actuation with an IDT, the domains should be aligned (uniformly or periodically) in the substrate plane, perpendicular to the IDT-electrodes.

Furthermore, we notice that a periodic orientation of the PZT domains (Figure 2c) results in a SAW resonance frequency (400 MHz) that is almost twice the SAW resonance frequency (202 MHz) from the PZT with all domains uniformly in-plane oriented (Figure 2b). This is because the actuation with an periodic domain polarity results in a SAW wavelength that is half of the IDT period, hence the resonance frequency doubles.

■ ACOUSTO-OPTIC INTERACTION

Next, we consider a PZT film integrated on an SOI photonic chip as schematically illustrated in Figure 1. The acoustic wave excited by the IDT results in a dynamic strain profile, which perturbs the refractive index of the medium (photoelastic effect). In the waveguide, this index modulation diffracts the incident carrier mode into two sidebands. After traveling through the modulator of length L, the modulated field can be described as (for details, see the Supporting Information)

$$\psi_1(t) = \Re A_1 \left\{ e^{i\omega_0 t} + \frac{\alpha(L)}{2} \left[e^{i(\omega_0+\Omega)t} - e^{i(\omega_0-\Omega)t} \right] \right\} \quad (1)$$

We thereby assumed that the modulator is short, thus the phase mismatch between the modulated signals (sidebands) and the carrier mode is negligible.

In this eq 1, A_1 is the electric field amplitude of the output light from the DUT (waveguide), ω_0 is the angular frequency of the incident light, Ω is the angular frequency of the acoustic wave, and $\alpha(L)$ is the phase modulation amplitude. $\alpha(L) = -(2\pi\Delta n_{\text{eff}} L/\lambda_0)$, where Δn_{eff} is the effective index change induced by the acoustic wave and λ_0 is the free space wavelength of the light. $\alpha(L)$ is a measure of the modulation efficiency and depends on the coupling between the induced acoustic field and the optical field in the waveguide.

To experimentally measure the optical phase modulation, we used a heterodyne setup as shown in Figure 3. The output signal of the modulator is combined with a frequency-shifted signal from an acousto-optic modulator (AOM) to down-convert the carrier signal in the photodetector. The frequency shifted signal exiting the AOM is given by

$$\psi_2(t) = \Re A_2 \{ e^{i(\omega_0+\Delta\omega)t} \} \quad (2)$$

where A_2 is the amplitude of the output light from AOM and $\Delta\omega = 2\pi \times 200$ MHz is the frequency shift induced by the AOM. Thus, the field coupled into the photodiode (PD) is

$$\psi_{\text{PD}}(t) = \psi_1(t) + \psi_2(t)$$

The output current from the PD, I_{PD} is equal to the responsivity of the PD times the optical input power $\Rightarrow I_{\text{PD}} \propto |\psi_{\text{PD}}|^2$. The electrical power measured by the ESA equals $P_{\text{ESA}} = I_{\text{PD}}^2 \times Z_0$, where Z_0 is the load impedance (50 Ω). Hence, the power spectrum measured in the ESA is given by

$$P_{\text{ESA}}(t) \propto \left[|A_1|^2 + |A_2|^2 + (A_1^* A_2 + A_2^* A_1) \left[\cos(\Delta\omega t) + \frac{\alpha(L)}{2} \{ \cos((\Delta\omega + \Omega)t) - \cos((\Delta\omega - \Omega)t) \} \right] + |A_1|^2 \alpha(L)^2 \sin^2(\Omega t) \right]^2 \quad (3)$$

We can ignore the last term, as $\alpha(L) \ll 1$, and unmodulated terms contributing only to the DC current. We then obtain

$$P_{\text{ESA}}(t) \propto 4|A_1|^2|A_2|^2 \times \left[\cos(\Delta\omega t) + \frac{\alpha(L)}{2} \{ \cos((\Delta\omega + \Omega)t) - \cos((\Delta\omega - \Omega)t) \} \right]^2 \quad (4)$$

The Fourier transform of eq 4 gives a peak signal at the AOM frequency shift $\Delta\omega$, and two sideband peaks at frequencies $|\Delta\omega \pm \Omega|$ are introduced by the acoustic wave modulation.

https://doi.org/10.1021/acsphotonics.1c01857
ACS Photonics 2022, 9, 1944−1953

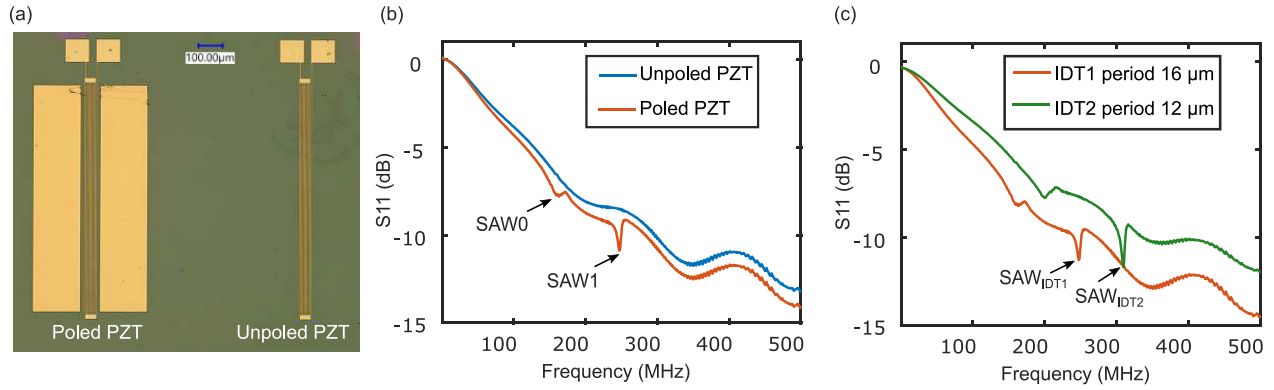

Figure 4. (a) Microscope image showing a test IDT fabricated in between parallel electrode bars (80 μm spacing) for poling process, and an identical control IDT fabricated without the electrode bars. (b) S_{11} signal measured for test (poled) and control (unpoled) IDT with a period of 16 μm. (c) S_{11} signal measured for poled IDTs with periods of 12 and 16 μm.

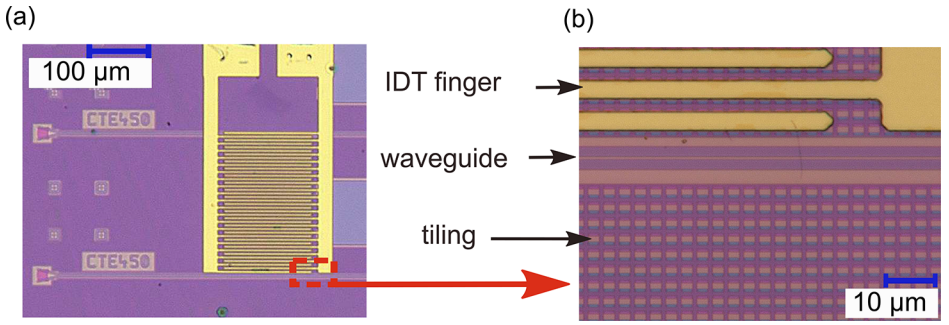

Figure 5. (a) Microscope image of an IDT with a finger-width of 3 μm, an aperture of 180 μm, and 20 finger-pairs, (b) zoomed-in image showing the tiling pattern (containing shallow and deep etched Si) distributed over the regions without waveguide designs. These 220 nm thick patterns have a periodicity of 3 μm and are defined in the Si-device layer to maintain uniformity during the wafer fabrication.

Further algebra on eq 4 gives us the following expression for the modulation amplitude $\alpha(L)$:

$$P_{\mathrm{ESA}}^{\mathrm{AOM}}[dBm] - P_{\mathrm{ESA}}^{\mathrm{sideband}}[dBm] = 20\log\left[\frac{\alpha(L)[\mathrm{rad}]}{2}\right] \quad (5)$$

Hence, the modulation amplitude $\alpha(L)$ can be extracted independent of the photodetector responsivity and gain. Now, with this $\alpha(L)$, we can calculate the voltage required for a π-phase shift $V_\pi = \pi V_{\mathrm{RF}}/\alpha(L)$, where V_{RF} is the voltage amplitude of the input RF signal.

For the power of the upper sideband peak in eq 4, we find

$$P_{\mathrm{ESA}}^{\mathrm{sideband}} \propto |A_1|^2|A_2|^2\alpha(L)^2(\cos((\Delta\omega + \Omega)t)) \Rightarrow P_{\mathrm{ESA}}^{\mathrm{sideband}} \propto P_{\mathrm{laser}}^2 P_{\mathrm{RF}}$$

As $\alpha(L)^2 \propto P_{\mathrm{RF}}$, where P_{RF} is the applied RF power to the IDT, and $|A_1|^2|A_2|^2 \propto P_{\mathrm{laser}}^2$, where P_{laser} is the input laser power. Thus, the above equation can be written as

$$P_{\mathrm{ESA}}^{\mathrm{sideband}}[dBm] = 2P_{\mathrm{laser}}[dBm] + P_{\mathrm{RF}}[dBm] + \mathrm{constant} \quad (6)$$

This shows how the modulated power depends on the input laser power and the driving RF power.

MATERIALS AND METHODS

We fabricated the PZT thin films by chemical solution deposition (CSD) as described in ref 68. The ultrathin (5−15 nm) lanthanide-based buffer layer ($La_2O_2CO_3$) used in this method works as an excellent lattice match, resulting in a uniform, crack-free, and preferentially c-oriented growth of the PZT thin film.[68] Moreover, this intermediate buffer layer provides an efficient diffusion barrier between the substrate and the PZT layer. After spin-coating the buffer solution on a substrate, we annealed the sample at 400−500 °C. Subsequently, we spin-coated the PZT precursor solution and subjected it to pyrolysis at 300 °C (we repeated this cycle to obtain a thicker PZT film). Then we annealed the amorphous PZT layer in a tube furnace at 500−600 °C for 20−30 min in oxygen ambient to let it crystallize. We finally obtained a PZT film with chemical composition $PbZr_{0.52}Ti_{0.48}O_3$.

To demonstrate the piezoelectric properties of our PZT film, we designed standalone IDT structures on PZT films deposited on a glass substrate. In a first fabrication step, we patterned parallel electrodes (separation 80−150 um) with laser direct write lithography (LDW), followed by deposition of a 20 nm Ti/350 nm Au layer through thermal evaporation and a lift-off process. These metal electrodes were used to uniformly pole the PZT film in-plane, for about 1 h at 40 °C. The applied DC voltage varied between 820 and 1100 V, depending on the electrodes separation. In the second step, we used the same metallization process for fabricating test IDTs (in the poled PZT region) and control IDTs (in the unpoled region), as shown in Figure 4a. The number of finger-pairs was limited to about 5−7 given the resolution of the optical lithography process and the limited spacing between the poling electrodes. On these IDTs, we measured the frequency dependent electrical reflection parameter S_{11} using a Fieldfox-vector network analyzer (VNA).

For characterizing the excitation of acoustic waves and their interaction with integrated waveguides, we used a SOI

https://doi.org/10.1021/acsphotonics.1c01857
ACS Photonics 2022, 9, 1944−1953

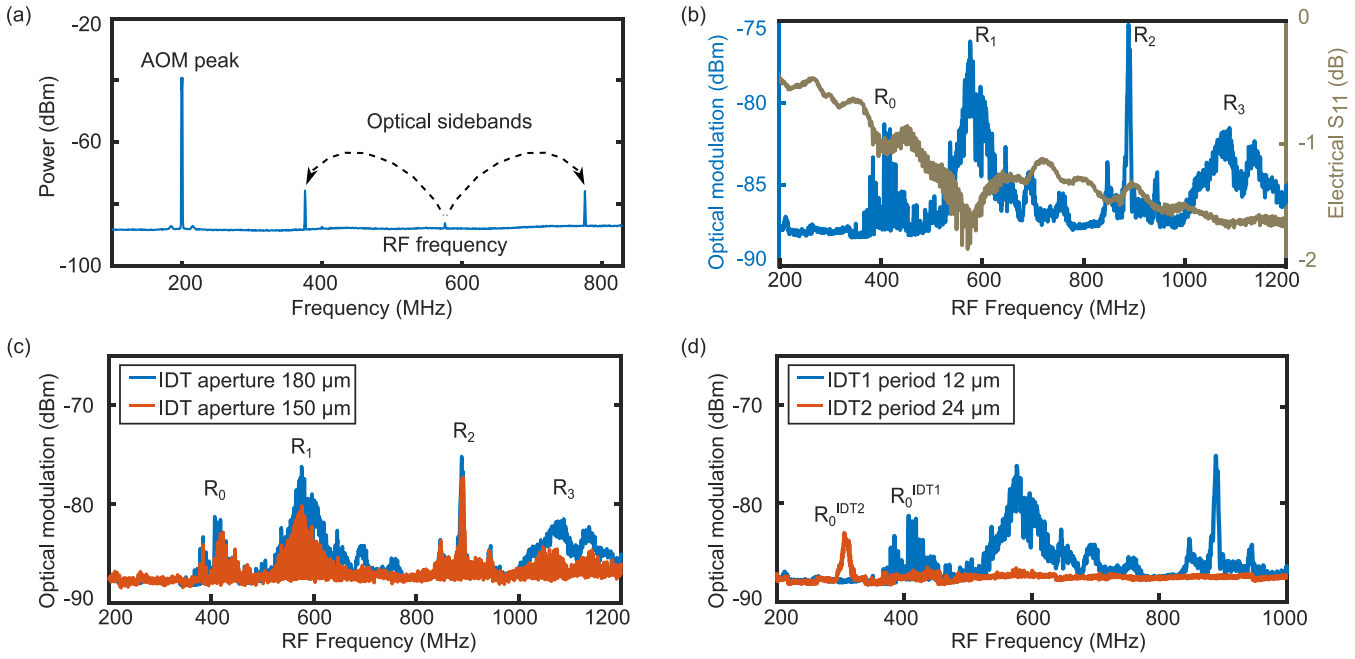

Figure 6. (a) Measured output spectrum for IDT with period 12 μm actuated with a 15 dBm RF signal at 576 MHz, showing the carrier peak at the AOM driving frequency (200 MHz) and optical sidebands at 576 ± 200 MHz. (b) Frequency dependent modulation spectrum (blue) and S_{11} (brown) for IDT with period 12 μm. The S_{11} spectrum shows dips at 410 and 576 MHz, while the measured optical modulation spectrum shows peaks at 410, 576, 888, and 1088 MHz. (c) Modulation spectra for IDT with aperture 180 and 150 μm. (d) Modulation spectra for IDT1 (with period of 12 μm, aperture 180 μm, 20 finger-pairs), placed 6 μm away from the waveguide, and IDT2 (with period 24 μm, aperture 280 μm, and 30 finger-pairs), placed 1024 μm away from the waveguide.

photonic chip, fabricated through a multiproject wafer (MPW) run, as the starting point. In the MPW fabrication process, the waveguides were defined in a 220 nm thick silicon layer on top of a 2 μm buried oxide layer. The chips were planarized using oxide deposition and chemical mechanical polishing (CMP). We deposited a 10−15 nm thick lanthanide-based buffer layer, followed by a 200 nm thick thick PZT-layer on these SOI chips. We then defined IDTs on top of the PZT layer using optical lithography, followed by deposition of 20 nm Ti/350 nm Au layer through thermal evaporation and a lift-off process as shown in Figure 5. Contrary to the approach taken for the glass substrate described in the previous paragraph, for these chips the PZT in the IDT region was poled using the IDT itself, by applying a voltage of 30−60 V (depending on the IDT-finger spacing) at 40 °C for about 40 min.

The experimental setup used for the measurement of the optical phase modulation is shown in Figure 3. The signal (1550 nm) from the laser (Santec TSL510) was divided into two parts by a 99/1 fiber splitter, with 1% of the signal routed through an acousto-optic modulator (Gooch & Housego Fiber-Q, driver model 1200 AF-AINA-2.5 HCR) to frequency-shift the signal by 200 MHz. The other 99% of the signal was fed into the DUT. A Rhodes & Schwarz-SMR40 signal generator was used as an RF source to actuate the IDT. The modulated signal from the waveguide was mixed with the output signal from the AOM via a 50/50 fiber combiner and fed into a fast TIA photodetector (Thorlab PDB480C or PD-40 GHz Discovery LabBuddy). The output of the PD was analyzed with an electrical spectrum analyzer (Agilent N9010A).

RESULTS AND DISCUSSIONS

In Figure 4a, we show a microscope image of a test IDT (between electrodes) and an identical, control IDT (without electrodes) fabricated on a PZT-on-glass substrate. The PZT film under the test IDT is uniformly in-plane poled (using the parallel electrodes), whereas for the control IDT, it is unpoled. Figure 4b shows the electrical reflection parameter S_{11} measured on the two types of IDTs (period 16 μm). We observe two dips at 161 and 247 MHz in the S_{11} measured on the test IDT and none from the control IDT. These dips indicate the actuation of acoustic waves because the input RF power is now converted into the acoustic power, lowering the reflected RF power. Therefore, this result already indicates that the IDT deposited on the poled PZT is more efficient in actuating acoustic waves compared to the IDT on as deposited (unpoled) PZT. Figure 4c shows the S_{11} response for two IDTs with different periods. We observed that the resonance frequencies shift proportionally with the IDT period. This corroborates that indeed the S_{11} dips are from the acoustic wave actuation as their excitation frequencies are determined by the IDT period. Thus, we conclude that our PZT film exhibits a piezo-electric effect and allows for the actuation of acoustic waves.

With the uniform in-plane poling scheme using an electrode-pair across the IDT pattern, the size of the poled PZT region is limited due to constraints on the maximum applicable voltage. Consequently, the size of the actuators is also limited. Therefore, in subsequent devices, we poled the PZT film using the IDT electrodes themselves.

Next, we characterized the strength of the acousto-optic interaction, using an SOI photonic chip with integrated PZT film. Figure 6a shows the output power spectrum when an IDT with period 12 μm is actuated with a 15 dBm RF signal at 576

https://doi.org/10.1021/acsphotonics.1c01857
ACS Photonics 2022, 9, 1944−1953

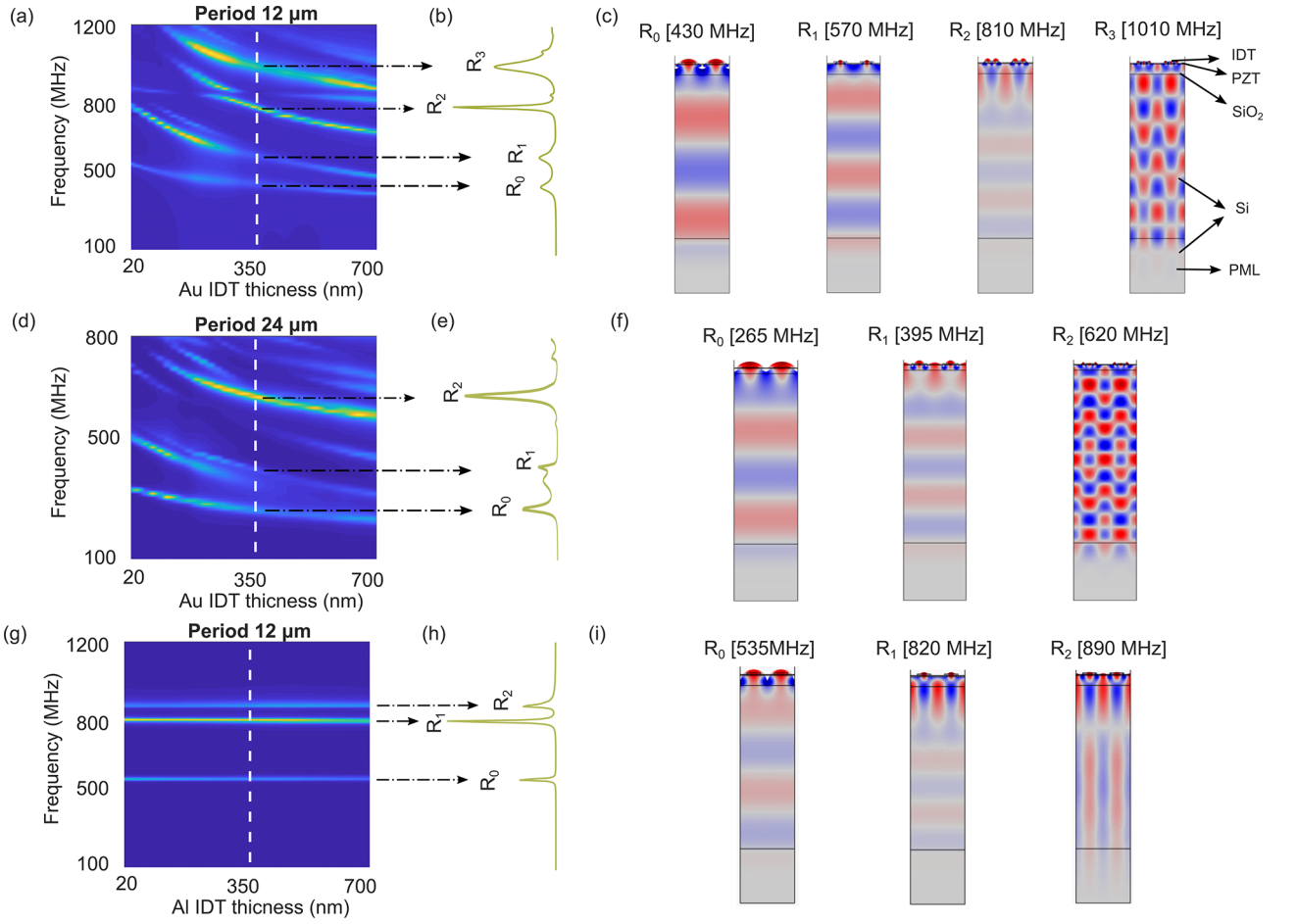

Figure 7. FEM calculated acoustic dispersion diagram with respect to the IDT thickness from a unit cell of (a) 12 μm period Au IDT, (d) 24 μm period Au IDT, and (g) 12 μm period Al IDT. The color map represents normalized elastic strain energy. (b, e, h) Elastic strain energy spectrum plotted for 350 nm IDT thickness. (c, f, i) Vertical-displacement profile of the corresponding modes for a 350 nm thick IDT. For the simulation details, see the Supporting Information.

MHz. As described in eq 4, the peak at 200 MHz corresponds to the AOM driving frequency and the two sidebands of the carrier, at 576 ± 200 MHz, result from the acousto-optic modulation. To characterize the modulation strength, we measured the amplitude of the upper sideband peak with respect to the applied RF frequency, for different IDTs, as shown in Figure 6b–d.

In Figure 6b, we compare the results from the optical modulation measured in the waveguide and the electrical S_{11} measured on the corresponding IDT (with period 12 μm and aperture 180 μm). We notice that the optical modulation peaks at 410 and 576 MHz are consistent with the transduction dips in the electrical S_{11} response. For the modulation peaks at 888 and 1088 MHz, however, we do not see clear dips in the S_{11} signal. We suspect this might be due to the additional noise or cross-talk at higher RF frequencies in the S_{11} measurement. Thus, both the electrical and optical measurements confirm the excitation of acoustic waves and the corresponding optical phase modulation in the waveguide.

In Figure 6c, we show the modulation spectra from devices with IDT aperture 180 and 150 μm. As expected, we see a proportional increment in the modulation strength when the modulation length (IDT aperture) is increased. In Figure 6d, we show the modulation spectra from devices with two different IDT periods. The spacing between the IDT aperture and the WG core edge is 6 μm for IDT1 (period 12 μm, no. of finger-pairs 20) and 1204 μm for IDT2 (period 24 μm, no. of finger-pairs 30). In the latter case (IDT2), the modulation spectrum shows only one peak while for IDT1 multiple peaks are visible. To understand this and get insight into the characteristics of the acoustic modes corresponding to these peaks, we carried out a detailed FEM simulation on a unit cell of the IDT, assuming periodic boundary conditions. The details of the simulation setup are discussed in the Supporting Information. Figure 7 shows the main results. In Figure 7a, we show the acoustic mode dispersion with respect to the thickness of a Au IDT (period 12 μm). Figure 7b shows the elastic energy spectrum for a thickness of 350 nm indicating four peaks, and the associated mode profiles are shown in Figure 7c. We note that R_0 at 430 MHz, R_1 at 570 MHz, R_2 at 810 MHz, and R_2 at 1010 MHz correspond to the fundamental SAW mode, a pseudo-SAW mode, a leaky-SAW mode, and a leaky mode. These can be linked to the peaks observed in the experimental spectrum shown in Figure 6c at 410, 576, 888, and 1088 MHz for IDT1. The small deviation between experimental and simulated results can be attributed to a slight mismatch in the geometric and material parameters used in the simulation and the real experiment. Additionally, the Si tiling pattern on the chip (see Figure 5) was not included in the simulation.

Similarly, Figure 7f, where the period was increased to 24 μm, shows the excitation of three main modes, whereby R_0 at

https://doi.org/10.1021/acsphotonics.1c01857
ACS Photonics 2022, 9, 1944–1953

265 MHz, R_1 at ∼395 MHz, and R_2 at 620 MHz correspond to the fundamental SAW mode, a pseudoleaky SAW mode, and a leaky mode, respectively. Given the leaky character of R_1 and R_2, only R_0 can travel a longer distance, explaining why we observed only a single modulation peak in Figure 6d for IDT2.

From the acoustic dispersion diagrams shown in Figure 7a,d, we notice that when the IDT thickness is negligible, there are three main modes excited: the fundamental SAW mode, a leaky-SAW mode, and a higher order (weak) SAW mode. However, when we increase the IDT thickness, the added mass-loading and grating reflection decreases the mode frequencies and introduces more leaky modes. While the mass-loading effect from the IDT can be desirable for some sensing applications,[69] in our case, it is undesirable as it weakens the SAW transduction strength and diffracts more energy into the substrate. As a result, the acousto-optic interaction in a WG in the surface layer gets weaker. To solve the problem of grating reflection, in some cases a split-finger IDT is used,[62,70] because the reflected waves from the grating then add up destructively. However, in case of periodic poling, this condition is not satisfied. Therefore, in our case, thinner and lower density metal electrodes could be a possible solution.

In Figure 7g we show the acoustic dispersion diagram for an Aluminum IDT, which has a low density (density ∼ 1/7 of Au) and lower acoustic impedance mismatch. Now we do not see any shift in the mode frequencies.

Therefore, in the next progression of fabrication, we used Al for designing the IDT. We used electron-beam lithography to pattern a small period IDT, which allows the excitation of higher (GHz) frequency acoustic waves. We deposited 100 nm thick Al using e-gun evaporation, followed by a metal-lift off process. Then we patterned additional contact pads with photolithography, followed by a ∼330 nm thick Al deposition and lift-off process. Finally, we covered the top of the device with a 50 nm Al_2O_3 layer using atomic-layer deposition (ALD). An example of the resulting devices is shown in the inset of Figure 8.

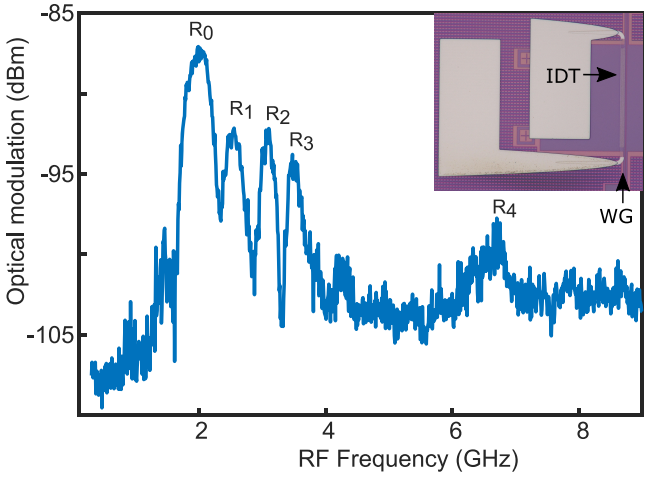

Figure 8. Measured optical modulation spectrum for an Al IDT with 4 finger-pairs, period 2 μm (finger-width 500 nm), and aperture length 70 μm, actuated with 12 dBm RF power. The spectrum shows modulation peaks at 2 GHz (R_0), 2.55 GHz (R_1), 3.1 GHz (R_2), 3.47 GHz (R_3), and 6.7 GHz (R_4). The inset shows a microscope image of the fabricated device, which was spaced 2 μm from the WG in a region without Si tiling.

Figure 8 shows the modulation spectrum measured from a 100 nm thick Al IDT with period 2 μm driven with 12 dBm of RF power. We find modulation peaks at 2 GHz (R_0), 2.5 GHz (R_1), 3.1 GHz (R_2), 3.5 GHz (R_3), and 6.7 GHz (R_4). From an FEM simulation, we conclude the first and the strongest modulation peak (R_0) to be the fundamental SAW mode,[53] while the other peaks belong to higher order modes.

In Figure 9 we show how the modulated power depends on the input laser power and the RF driving power. These

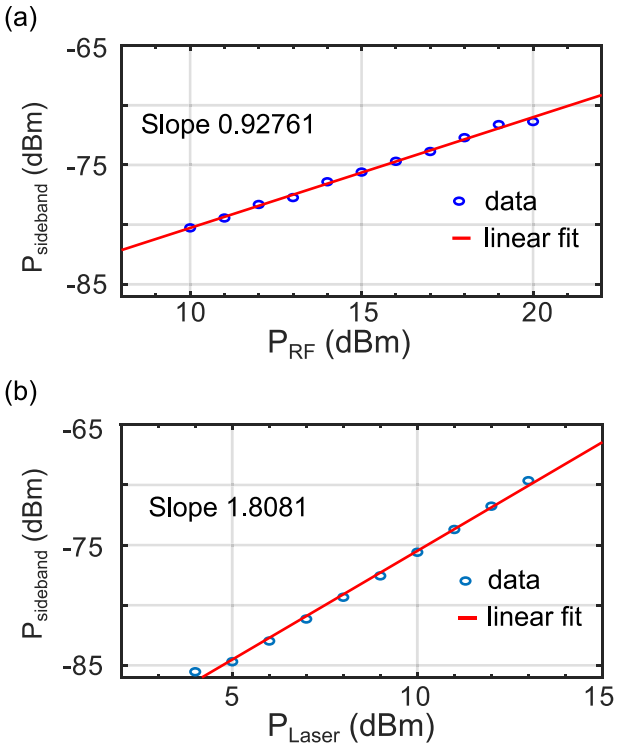

Figure 9. Modulated power (sideband peak) dependence on (a) the driving RF power at a fixed laser input of 10 dBm and (b) the laser power at a fixed RF power of 15 dBm. The measurement was done on the IDT of period 12 μm at an RF frequency of 576 MHz.

measurements were done on the IDT of period 12 μm at an RF frequency of 576 MHz. The slopes obtained from a linear fit of the data are very close to the expected values, as discussed in eq 6. The small deviation is attributed mainly to the higher order terms in the phase modulation, which are not negligible anymore at higher RF power, and poor signal-to-noise ratio at lower optical power.

From comparing the AOM peak (−39.15 dBm) and the modulation peak (−75.60 dBm) in Figure 6a, we extract the phase modulation amplitude $\alpha(L)$ using eq 5. We obtained $\alpha(L)$ to be ≈0.03 rad, when the Au IDT with period 12 μm, 20 finger-pairs and aperture of 180 μm is actuated with 15 dBm RF power at 576 MHz. The corresponding $V_\pi L$ is ≈3.35 V·cm. Similarly, for the Al IDT of period 2 μm and aperture 70 μm, the modulation peak at 2 GHz (R_0) was measured to be at −87.3 dBm (Figure 8), while the AOM peak was noted at −43.5 dBm. This gives $\alpha(L) \approx 0.0077$ rad and the corresponding $V_\pi L$ to be ≈3.60 V·cm. This is a significant improvement considering that the Al IDT now consists of only four finger-pairs. While we believe the main reason for this improvement is a low mass-loading and grating reflection from the Al IDT, as discussed above, the other contributing factors

https://doi.org/10.1021/acsphotonics.1c01857
ACS Photonics 2022, 9, 1944−1953

could be the absence of the Si tiling pattern and a stronger acousto-optic overlap in the waveguide (width 0.45 μm) from the acoustic wave (wavelength ∼1 μm).

With a similar PZT layer, a modulator exploiting the electro-optic (EO) effect has been reported to exhibit $V_\pi L \approx 3.2$ V·cm.[48] In ref 20, using a Si waveguide integrated with AlN and an IDT consisting of 107 finger-pairs actuated at 3.11 GHz, the $V_\pi L$ was reported to be 1.8 V·cm. Thus, our figures of merit are competitive to state-of-the-art electro-optic and acousto-optic modulators integrated on Si PICs.

CONCLUSION

We investigated the piezo-electrical actuation of surface acoustic waves using a photonic compatible PZT film. Then we integrated a PZT thin film on a planarized SOI photonic chip to induce acousto-optic modulation in a waveguide with MHz acoustic waves from the Au IDT. Thereafter, through FEM analysis, we pointed out the issue of mass-loading and grating reflection from the Au IDT. We then fabricated a new device with an Al IDT and smaller period to actuate GHz acoustic waves. We obtained a competitive $V_\pi L \approx 3.6$ V·cm with an Al IDT consisting of only 4 finger-pairs, without patterning the PZT layer or under-etching the device. Further improvements in the device performance are expected when the scattering and damping loss factors are eliminated. For instance, the IDT design can be optimized to match the electrical impedance, thus minimize the RF power reflection. Additionally, the current bidirectional IDT actuates the acoustic waves in both directions, thus only half of the acoustic energy is utilized for the modulation. We can define an acoustic reflector to collect the other half or design a unidirectional SAW actuator.[71,72] Furthermore, to avoid leakage of any acoustic energy into the substrate and any interference from the bulk acoustic waves, the device could be underetched.

Thus, we demonstrated that our PZT film, deposited on planarized silicon photonics chips, exhibits a strong piezo-electric effect and can be exploited to achieve strong phonon-photon coupling in microscale waveguides. Through this hybrid integration process, we hope to realize power efficient, miniaturized, and scalable piezoelectric microactuator-based photonic components such as tunable filters, isolators, modulators, switches, and beam-steering.

ASSOCIATED CONTENT

Supporting Information

The Supporting Information is available free of charge at https://pubs.acs.org/doi/10.1021/acsphotonics.1c01857.

Simulation procedure for the acoustic wave actuation and analytical analysis of the acousto-optic interaction in a waveguide (PDF)

AUTHOR INFORMATION

Corresponding Author

Dries Van Thourhout − *Centre for Nano and Bio-photonics, Ghent University, 9052 Ghent, Belgium; Photonics Research Group, INTEC, Ghent University-IMEC, 9052 Ghent, Belgium;* orcid.org/0000-0003-0111-431X; Email: dries.vanthourhout@UGent.be

Authors

Irfan Ansari − *Centre for Nano and Bio-photonics and Liquid Crystal and Photonics Group, ELIS, Ghent University, 9052 Ghent, Belgium; Photonics Research Group, INTEC, Ghent University-IMEC, 9052 Ghent, Belgium*

John P. George − *Centre for Nano and Bio-photonics and Liquid Crystal and Photonics Group, ELIS, Ghent University, 9052 Ghent, Belgium; Photonics Research Group, INTEC, Ghent University-IMEC, 9052 Ghent, Belgium*

Gilles F. Feutmba − *Centre for Nano and Bio-photonics and Liquid Crystal and Photonics Group, ELIS, Ghent University, 9052 Ghent, Belgium; Photonics Research Group, INTEC, Ghent University-IMEC, 9052 Ghent, Belgium*

Tessa Van de Veire − *Centre for Nano and Bio-photonics and Liquid Crystal and Photonics Group, ELIS, Ghent University, 9052 Ghent, Belgium*

Awanish Pandey − *Centre for Nano and Bio-photonics, Ghent University, 9052 Ghent, Belgium; Photonics Research Group, INTEC, Ghent University-IMEC, 9052 Ghent, Belgium*

Jeroen Beeckman − *Centre for Nano and Bio-photonics and Liquid Crystal and Photonics Group, ELIS, Ghent University, 9052 Ghent, Belgium;* orcid.org/0000-0002-0711-2465

Complete contact information is available at: https://pubs.acs.org/10.1021/acsphotonics.1c01857

Funding

This work was supported by the EU commission through Grant Agreement No. 732894 (FET proactive HOT) and through the UGent Grant BOFGOA2020000103. G.F.F. acknowledges support and funding as an SB-PhD Fellow of the research foundation Flanders (FWO, Grant Number 1S68218N).

Notes

The authors declare no competing financial interest.

REFERENCES

(1) Marpaung, D.; Roeloffzen, C.; Heideman, R.; Leinse, A.; Sales, S.; Capmany, J. Integrated microwave photonics. *Laser & Photonics Reviews* **2013**, *7*, 506−538.

(2) Marpaung, D.; Morrison, B.; Pagani, M.; Pant, R.; Choi, D.-Y.; Luther-Davies, B.; Madden, S. J.; Eggleton, B. J. Low-power, chip-based stimulated Brillouin scattering microwave photonic filter with ultrahigh selectivity. *Optica* **2015**, *2*, 76−83.

(3) Kang, M. S.; Butsch, A.; Russell, P. S. J. Reconfigurable light-driven opto-acoustic isolators in photonic crystal fibre. *Nat. Photonics* **2011**, *5*, 549−553.

(4) Yu, Z.; Fan, S. Complete optical isolation created by indirect interband photonic transitions. *Nat. Photonics* **2009**, *3*, 91−94.

(5) Huang, D.; Pintus, P.; Zhang, C.; Shoji, Y.; Mizumoto, T.; Bowers, J. E. Electrically driven and thermally tunable integrated optical isolators for silicon photonics. *IEEE J. Sel. Top. Quantum Electron.* **2016**, *22*, 271−278.

(6) Sohn, D. B.; Bahl, G. Direction reconfigurable nonreciprocal acousto-optic modulator on chip. *APL Photonics* **2019**, *4*, 126103.

(7) Fan, L.; Zou, C.-L.; Poot, M.; Cheng, R.; Guo, X.; Han, X.; Tang, H. X. Integrated optomechanical single-photon frequency shifter. *Nat. Photonics* **2016**, *10*, 766−770.

(8) Tadesse, S. A.; Li, M. Sub-optical wavelength acoustic wave modulation of integrated photonic resonators at microwave frequencies. *Nat. Commun.* **2014**, *5*, 1−7.

(9) Tadesse, S. A.; Li, H.; Liu, Q.; Li, M. Acousto-optic modulation of a photonic crystal nanocavity with Lamb waves in microwave K band. *Appl. Phys. Lett.* **2015**, *107*, 201113.

(10) Balram, K. C.; Davanço, M. I.; Ilic, B. R.; Kyhm, J.-H.; Song, J. D.; Srinivasan, K. Acousto-optic modulation and optoacoustic gating

in piezo-optomechanical circuits. *Physical review applied* **2017**, *7*, 024008.
(11) de Lima, M., Jr; Beck, M.; Hey, R.; Santos, P. Compact Mach-Zehnder acousto-optic modulator. *Applied physics letters* **2006**, *89*, 121104.
(12) Hassanien, A. E.; Link, S.; Yang, Y.; Chow, E.; Goddard, L. L.; Gong, S. Efficient and wideband acousto-optic modulation on thin-film lithium niobate for microwave-to-photonic conversion. *Photon. Res.* **2021**, *9*, 1182−1190.
(13) Yu, Z.; Sun, X. Gigahertz Acousto-Optic Modulation and Frequency Shifting on Etchless Lithium Niobate Integrated Platform. *ACS Photonics* **2021**, *8*, 798−803.
(14) Kuhn, L.; Heidrich, P.; Lean, E. Optical guided wave mode conversion by an acoustic surface wave. *Appl. Phys. Lett.* **1971**, *19*, 428−430.
(15) Sasaki, H.; Kushibiki, J.; Chubachi, N. Efficient acousto-optic TE-TM mode conversion in ZnO films. *Appl. Phys. Lett.* **1974**, *25*, 476−477.
(16) Ohmachi, Y.; Noda, J. LiNbO 3 TE-TM mode converter using collinear acoustooptic interaction. *IEEE J. Quantum Electron.* **1977**, *13*, 43−46.
(17) Safavi-Naeini, A. H.; Van Thourhout, D.; Baets, R.; Van Laer, R. Controlling phonons and photons at the wavelength scale: integrated photonics meets integrated phononics. *Optica* **2019**, *6*, 213−232.
(18) Sohn, D. B.; Kim, S.; Bahl, G. Time-reversal symmetry breaking with acoustic pumping of nanophotonic circuits. *Nat. Photonics* **2018**, *12*, 91−97.
(19) Kittlaus, E. A.; Otterstrom, N. T.; Kharel, P.; Gertler, S.; Rakich, P. T. Non-reciprocal interband Brillouin modulation. *Nat. Photonics* **2018**, *12*, 613−619.
(20) Kittlaus, E. A.; Jones, W. M.; Rakich, P. T.; Otterstrom, N. T.; Muller, R. E.; Rais-Zadeh, M. Electrically driven acousto-optics and broadband non-reciprocity in silicon photonics. *Nat. Photonics* **2021**, *15*, 43−52.
(21) Jessen, P.; Kristensen, M. Generation of a frequency comb with a double acousto-optic modulator ring. *Appl. Opt.* **1992**, *31*, 4911−4913.
(22) Durán, V.; De Chatellus, H. G.; Schnebélin, C.; Nithyanandan, K.; Djevarhidjian, L.; Clement, J.; Fernández-Pousa, C. R. Optical Frequency Combs Generated by Acousto-Optic Frequency-Shifting Loops. *IEEE Photonics Technology Letters* **2019**, *31*, 1878−1881.
(23) Shao, L.; Sinclair, N.; Leatham, J.; Hu, Y.; Yu, M.; Turpin, T.; Crowe, D.; Lončar, M. Integrated microwave acousto-optic frequency shifter on thin-film lithium niobate. *Opt. Express* **2020**, *28*, 23728−23738.
(24) Aspelmeyer, M.; Kippenberg, T. J.; Marquardt, F. Cavity optomechanics. *Rev. Mod. Phys.* **2014**, *86*, 1391−1452.
(25) Andrews, R. W.; Peterson, R. W.; Purdy, T. P.; Cicak, K.; Simmonds, R. W.; Regal, C. A.; Lehnert, K. W. Bidirectional and efficient conversion between microwave and optical light. *Nat. Phys.* **2014**, *10*, 321−326.
(26) Verhagen, E.; Deléglise, S.; Weis, S.; Schliesser, A.; Kippenberg, T. J. Quantum-coherent coupling of a mechanical oscillator to an optical cavity mode. *Nature* **2012**, *482*, 63−67.
(27) Nysten, E. D. S.; Huo, Y. H.; Yu, H.; Song, G. F.; Rastelli, A.; Krenner, H. J. Multi-harmonic quantum dot optomechanics in fused LiNbO3−(Al)GaAs hybrids. *J. Phys. D: Appl. Phys.* **2017**, *50*, 43LT01.
(28) Kapfinger, S.; Reichert, T.; Lichtmannecker, S.; Müller, K.; Finley, J. J.; Wixforth, A.; Kaniber, M.; Krenner, H. J. Dynamic acousto-optic control of a strongly coupled photonic molecule. *Nat. Commun.* **2015**, *6*, 1−6.
(29) Cai, L.; Mahmoud, A.; Piazza, G. Low-loss waveguides on Y-cut thin film lithium niobate: towards acousto-optic applications. *Opt. Express* **2019**, *27*, 9794−9802.
(30) Shao, L.; Yu, M.; Maity, S.; Sinclair, N.; Zheng, L.; Chia, C.; Shams-Ansari, A.; Wang, C.; Zhang, M.; Lai, K.; Lončar, M. Microwave-to-optical conversion using lithium niobate thin-film acoustic resonators. *Optica* **2019**, *6*, 1498−1505.
(31) Sarabalis, C. J.; McKenna, T. P.; Patel, R. N.; Van Laer, R.; Safavi-Naeini, A. H. Acousto-optic modulation in lithium niobate on sapphire. *APL Photonics* **2020**, *5*, 086104.
(32) de Lima, M. M.; Beck, M.; Hey, R.; Santos, P. V. Compact Mach-Zehnder acousto-optic modulator. *Appl. Phys. Lett.* **2006**, *89*, 121104.
(33) Beck, M.; de Lima, M. M.; Wiebicke, E.; Seidel, W.; Hey, R.; Santos, P. V. Acousto-optical multiple interference switches. *Appl. Phys. Lett.* **2007**, *91*, 061118.
(34) Balram, K. C.; Davanço, M. I.; Ilic, B. R.; Kyhm, J.-H.; Song, J. D.; Srinivasan, K. Acousto-Optic Modulation and Optoacoustic Gating in Piezo-Optomechanical Circuits. *Phys. Rev. Applied* **2017**, *7*, 024008.
(35) Sun, B.; Kar-Roy, A.; Tsai, C. S. Guided-Wave Acousto-Optic Bragg Diffractions in InP/InGaAsP/InP Waveguide. *Integrated Photonics Research* **1995**, IThG15.
(36) Makles, K.; Antoni, T.; Kuhn, A. G.; Deléglise, S.; Briant, T.; Cohadon, P.-F.; Braive, R.; Beaudoin, G.; Pinard, L.; Michel, C.; Dolique, V.; Flaminio, R.; Cagnoli, G.; Robert-Philip, I.; Heidmann, A. 2D photonic-crystal optomechanical nanoresonator. *Opt. Lett.* **2015**, *40*, 174−177.
(37) Jalali, B.; Fathpour, S. Silicon Photonics. *Journal of Lightwave Technology* **2006**, *24*, 4600−4615.
(38) Bogaerts, W.; Baets, R.; Dumon, P.; Wiaux, V.; Beckx, S.; Taillaert, D.; Luyssaert, B.; Van Campenhout, J.; Bienstman, P.; Van Thourhout, D. Nanophotonic waveguides in silicon-on-insulator fabricated with CMOS technology. *Journal of Lightwave Technology* **2005**, *23*, 401−412.
(39) Munk, D.; Katzman, M.; Hen, M.; Priel, M.; Feldberg, M.; Sharabani, T.; Levy, S.; Bergman, A.; Zadok, A. Surface acoustic wave photonic devices in silicon on insulator. *Nat. Commun.* **2019**, *10*, 4214.
(40) Katzman, M.; Munk, D.; Priel, M.; Grunwald, E.; Hen, M.; Inbar, N.; Feldberg, M.; Sharabani, T.; Zektzer, R.; Bashan, G.; Vofsi, M.; Levy, U.; Zadok, A. Surface acoustic microwave photonic filters in standard silicon-on-insulator. *Optica* **2021**, *8*, 697−707.
(41) Xiong, C.; Pernice, W. H. P.; Sun, X.; Schuck, C.; Fong, K. Y.; Tang, H. X. Aluminum nitride as a new material for chip-scale optomechanics and nonlinear optics. *New J. Phys.* **2012**, *14*, 095014.
(42) Auld, B. A. *Acoustic Fields and Waves in Solids*; John Wiley & Sons, 1973.
(43) Safaei, M.; Sodano, H. A.; Anton, S. R. A review of energy harvesting using piezoelectric materials: state-of-the-art a decade later (2008−2018). *Smart Materials and Structures* **2019**, *28*, 113001.
(44) JAFFE, H. Piezoelectric Ceramics. *J. Am. Ceram. Soc.* **1958**, *41*, 494−498.
(45) Izyumskaya, N.; Alivov, Y.-I.; Cho, S.-J.; Morkoç, H.; Lee, H.; Kang, Y.-S. Processing, Structure, Properties, and Applications of PZT Thin Films. *Critical Reviews in Solid State and Materials Sciences* **2007**, *32*, 111−202.
(46) Hosseini, N.; Dekker, R.; Hoekman, M.; Dekkers, M.; Bos, J.; Leinse, A.; Heideman, R. Stress-optic modulator in TriPleX platform using a piezoelectric lead zirconate titanate (PZT) thin film. *Opt. Express* **2015**, *23*, 14018−14026.
(47) George, J. P.; Smet, P. F.; Botterman, J.; Bliznuk, V.; Woestenborghs, W.; Van Thourhout, D.; Neyts, K.; Beeckman, J. Lanthanide-Assisted Deposition of Strongly Electro-optic PZT Thin Films on Silicon: Toward Integrated Active Nanophotonic Devices. *ACS Appl. Mater. Interfaces* **2015**, *7*, 13350−13359.
(48) Alexander, K.; George, J. P.; Verbist, J.; Neyts, K.; Kuyken, B.; Van Thourhout, D.; Beeckman, J. Nanophotonic Pockels modulators on a silicon nitride platform. *Nat. Commun.* **2018**, *9*, 4−9.
(49) Feutmba, G. F.; de Veire, T. V.; Ansari, I.; George, J. P.; Thourhout, D. V.; Beeckman, J. A Strong Pockels PZT/Si Modulator for Efficient Electro-Optic Tuning. *OSA Advanced Photonics Congress (AP) 2020* (IPR, NP, NOMA, Networks, PVLED, PSC, SPPCom, SOF), Optica Publishing Group, 2020; p ITu1A.6.
(50) Feutmba, G. F.; Hermans, A.; George, J. P.; Rijckaert, H.; Ansari, I.; Van Thourhout, D.; Beeckman, J. Reversible and Tunable

https://doi.org/10.1021/acsphotonics.1c01857
ACS Photonics 2022, 9, 1944−1953

Second-Order Nonlinear Optical Susceptibility in PZT Thin Films for Integrated Optics. *Advanced Optical Materials* **2021**, *9*, 2100149.
(51) Ansari, I.; de Veire, T. V.; George, J. P.; Feutmba, G.; Beeckman, J.; Thourhout, D. V. Si-photonic integrated PZT thin film for acousto-optic modulation. *Conference on Lasers and Electro-Optics*, IEEE, 2020; p JTh2B.24.
(52) van der Slot, P. J. M.; Porcel, M. A. G.; Boller, K.-J. Surface acoustic waves for acousto-optic modulation in buried silicon nitride waveguides. *Opt. Express* **2019**, *27*, 1433−1452.
(53) Ansari, I.; Thourhout, D. V.; George, J. P.; Feutmba, G. F.; Beeckman, J. Acousto-optic modulation in a Si-waveguide. *2021 IEEE 17th International Conference on Group IV Photonics (GFP)*, IEEE, 2021; pp 1−2.
(54) Crespo-Poveda, A.; Hey, R.; Biermann, K.; Tahraoui, A.; Santos, P. V.; Gargallo, B.; Munoz, P.; Cantarero, A.; de Lima, M. M. Synchronized photonic modulators driven by surface acoustic waves. *Opt. Express* **2013**, *21*, 21669−21676.
(55) Rayleigh, L. On Waves Propagated along the Plane Surface of an Elastic Solid. *Proceedings of the London Mathematical Society* **1885**, *s1−17*, 4−11.
(56) Milsom, R.; Reilly, N.; Redwood, M. Analysis of Generation and Detection of Surface and Bulk Acoustic Waves by Interdigital Transducers. *IEEE Transactions on Sonics and Ultrasonics* **1977**, *24*, 147−166.
(57) Slobodnik, A. Surface acoustic waves and SAW materials. *Proceedings of the IEEE* **1976**, *64*, 581−595.
(58) Giannetti, C.; Revaz, B.; Banfi, F.; Montagnese, M.; Ferrini, G.; Cilento, F.; Maccalli, S.; Vavassori, P.; Oliviero, G.; Bontempi, E.; Depero, L. E.; Metlushko, V.; Parmigiani, F. Thermomechanical behavior of surface acoustic waves in ordered arrays of nanodisks studied by near-infrared pump-probe diffraction experiments. *Phys. Rev. B* **2007**, *76*, 125413.
(59) Nardi, D.; Travagliati, M.; Siemens, M. E.; Li, Q.; Murnane, M. M.; Kapteyn, H. C.; Ferrini, G.; Parmigiani, F.; Banfi, F. Probing Thermomechanics at the Nanoscale: Impulsively Excited Pseudosurface Acoustic Waves in Hypersonic Phononic Crystals. *Nano Lett.* **2011**, *11*, 4126−4133.
(60) Schubert, M.; Grossmann, M.; Ristow, O.; Hettich, M.; Bruchhausen, A.; Barretto, E. C. S.; Scheer, E.; Gusev, V.; Dekorsy, T. Spatial-temporally resolved high-frequency surface acoustic waves on silicon investigated by femtosecond spectroscopy. *Appl. Phys. Lett.* **2012**, *101*, 013108.
(61) Campbell, C. *Surface Acoustic Wave Devices for Mobile and Wireless Communications, Four-Vol. Set*; Academic Press, 1998.
(62) Royer, D.; Dieulesaint, E. *Elastic waves in solids II: generation, acousto-optic interaction, applications*; Springer Science & Business Media, 1999.
(63) Zheng, J.; Zhou, J.; Zeng, P.; Liu, Y.; Shen, Y.; Yao, W.; Chen, Z.; Wu, J.; Xiong, S.; Chen, Y.; Shi, X.; Liu, J.; Fu, Y.; Duan, H. 30 GHz surface acoustic wave transducers with extremely high mass sensitivity. *Appl. Phys. Lett.* **2020**, *116*, 123502.
(64) Oshio, M.; Kanna, S.; Iizawa, K. Effect of substrate thickness on quasi-longitudinal leaky SAW propagation on quartz. *IEEE Ultrasonics Symposium*, IEEE, 2005; pp 1880−1883.
(65) Kratzer, M.; Lasnik, M.; Röhrig, S.; Teichert, C.; Deluca, M. Reconstruction of the domain orientation distribution function of polycrystalline PZT ceramics using vector piezoresponse force microscopy. *Scientific Reports 2017 8:1* **2018**, *8*, 1−11.
(66) IEEE Standard on Piezoelectricity. *ANSI/IEEE Std 176−1987*; IEEE, 1988, DOI: 10.1109/IEEESTD.1988.79638.
(67) Butt, Z.; Pasha, R. A.; Qayyum, F.; Anjum, Z.; Ahmad, N.; Elahi, H. Generation of electrical energy using lead zirconate titanate (PZT-5A) piezoelectric material: Analytical, numerical and experimental verifications. *Journal of Mechanical Science and Technology* **2016**, *30*, 3553−3558.
(68) George, J. P.; Smet, P. F.; Botterman, J.; Bliznuk, V.; Woestenborghs, W.; Van Thourhout, D.; Neyts, K.; Beeckman, J. Lanthanide-Assisted Deposition of Strongly Electro-optic PZT Thin Films on Silicon: Toward Integrated Active Nanophotonic Devices. *ACS Appl. Mater. Interfaces* **2015**, *7*, 13350−13359.
(69) Chen, Z.; Zhou, J.; Tang, H.; Liu, Y.; Shen, Y.; Yin, X.; Zheng, J.; Zhang, H.; Wu, J.; Shi, X.; et al. Ultrahigh-frequency surface acoustic wave sensors with giant mass-loading effects on electrodes. *ACS Sensors* **2020**, *5*, 1657−1664.
(70) Crespo-Poveda, A.; Hey, R.; Biermann, K.; Tahraoui, A.; Santos, P.; Gargallo, B.; Muñoz, P.; Cantarero, A.; de Lima, M. Synchronized photonic modulators driven by surface acoustic waves. *Opt. Express* **2013**, *21*, 21669−21676.
(71) Ekström, M. K.; Aref, T.; Runeson, J.; Björck, J.; Boström, I.; Delsing, P. Surface acoustic wave unidirectional transducers for quantum applications. *Appl. Phys. Lett.* **2017**, *110*, 073105.
(72) Dumur, E.; Satzinger, K. J.; Peairs, G. A.; Chou, M.-H.; Bienfait, A.; Chang, H.-S.; Conner, C. R.; Grebel, J.; Povey, R. G.; Zhong, Y. P.; Cleland, A. N. Unidirectional distributed acoustic reflection transducers for quantum applications. *Appl. Phys. Lett.* **2019**, *114*, 223501.

https://doi.org/10.1021/acsphotonics.1c01857
ACS Photonics 2022, 9, 1944−1953